POLISH MARITIME RESEARCH 3 (123) 2024 Vol. 31; pp. 113-125
10.2478/pomr-2024-0041

A Novel Approach to Wave Energy Conversion Using CFD Technique

Nawar Abbas [1] *
Michel Barbahan [1]
Yako Kabrial [2]
Admoun Kabrial [2]
[1] Tishreen University Department of Maritime Engineering, Latakia, Syrian Arab Republic
[2] Scand Wave organization 559258-6357. Ängsvägen 17, 55633 Jönköping, Sweden

* Corresponding author: *noarabbas@yahoo.com (Nawar Abbas)*

ABSTRACT

This article details the development and evaluation of a novel wave energy converter (WEC) aimed at efficiently capturing wave energy for electricity production. The study employs Computational Fluid Dynamics (CFD) techniques, specifically the URANS method and the k-ω SST turbulence model, to solve the Navier-Stokes equations and capture the free surface using the Volume of Fluid (VOF) model. The CFD results are validated against experimental data to ensure accuracy. Various design parameters of the proposed device were tested, revealing that the arms and bottom angle significantly affect its performance. Unlike the floating Wave Dragon (WD) device, which utilises potential energy and is set in deep water, the new fixed-seabed device is positioned in the transitional wave region near the shore, where waves retain 80% of their energy. It can be constructed from environmentally friendly cement, making it resistant to hurricanes and suitable for any wave turbine in the open sea. The MP687 turbine was used to capture the wave energy in the proposed device, testing its performance in three positions: in the open sea, in the middle of the device, and at the device's outlet. The results show that the device significantly enhances wave energy concentration, especially when the turbine is placed at the outlet. The proposed device offers numerous advantages, including its fixed position in a high-energy wave zone, the efficient use of turbulent kinetic energy, and robust construction that can withstand storms.

Keywords: marine renewable energy, wave energy converters, CFD, URANS, MP687

INTRODUCTION

Among the major pillars of stability and prosperity, the energy sector sustains cities, drives industries, and propels economies. Conventional energy sources like oil, coal, and natural gas have been successful in promoting economic growth. Nevertheless, due to their diminishing availability and rising energy needs, global primary energy usage increased by 1.8% in 2012 [1]. In order to meet this growing demand, it is crucial to explore alternative sources of power, particularly in the form of electricity. Another significant concern is the preservation of our environment. Using fossil fuels for power generation releases large amounts of carbon dioxide (CO_2), poses risks to public health, and causes environmental harm. It is important to note that fossil fuels are finite resources and their use threatens future generations. Scientists worldwide actively seek sustainable development strategies to generate power for societal progress while preserving resources for future generations and minimising environmental impact as much as possible [2].

Wave energy is a form of renewable energy generated by the movement of ocean waves. It is a clean energy source that can potentially deliver significant electricity to coastal communities worldwide. Utilising wave energy is not new, as the original patent was first introduced in 1799 [3].

The technology used to harness wave energy is called a wave energy converter (WEC), which is typically installed offshore and consists of a device that captures the kinetic energy of the waves and converts it into electricity. There are several types of WECs, including point absorbers (PAs), attenuator-types WECs (AWECs), oscillating water columns (OWCs), and terminator-types WECs (TWECs). Terminators are oriented perpendicular to the wave direction, typically including duck-like devices, oscillating wave surge converters (OWSCs) and overtopping devices. [4]. This paper focuses on Wave Dragon (WD) devices, which are among the overtopping devices [5-7]. Several studies have been conducted on WD technology, to assess its performance and potential. A study by Kofoed et al. (2006) [8] investigated the hydrodynamic performance of a scaled-down model of a Wave Dragon device. The study found that the device could capture a significant amount of wave energy and convert it into electricity, with an efficiency of up to 60%. Another study, by Falcao 2010 [9], investigated the power output of a Wave Dragon device in various sea states. The study found that the device could generate significant power, even in low wave conditions and can be deployed usefully in many locations.

The study by Parmeggiani et al. 2013 [10] discussed an experimental update to the overtopping model used for the wave energy converter, which could improve wave energy conversion efficiency. The study by Parmeggiani et al. emphasised the importance of developing renewable energy sources, like wave energy, to reduce reliance on fossil fuels and mitigate climate change.

The use of constructal design in an overtopping wave energy converter was discussed in the study by Martins et al. (2018) [11], to evaluate the main operating principle of this device. This involved analyzing the geometric aspects of the device and optimising its design to maximise energy conversion efficiency. The study found that the overtopping wave energy converter has significant potential for generating renewable energy and that constructal design can effectively improve its performance.

In this study, the authors aim to develop one of the known methods for capturing and converting wave energy into electrical energy.

The remainder of this paper is organised as follows: the second section briefly reviews the numerical method implemented in this work, to compute wave flow. In the third section, the authors validate the numerical method using MP687 propeller test cases. Next, the geometry of the proposed device, as well as the configuration and numerical environment, are described. A summary of the results is demonstrated in the final section.

MATERIALS AND METHODS

GOVERNING EQUATIONS

The Navier-Stokes equations and the continuity equation were used to solve the problem. When the Reynolds averaging method is used to model turbulence, the Navier-Stokes equations can be expressed in a Cartesian tensor form, as follows:

$$\frac{\partial \rho}{\partial t} + \frac{\partial(\rho u_i)}{\partial x_i} = 0$$

$$\frac{\partial(\rho u_i)}{\partial t} + \frac{\partial}{\partial x_j}(\rho u_i u_j) = \frac{\partial \bar{p}}{\partial x_j} + \frac{\partial}{\partial x_j}\mu\left(\frac{\partial u_i}{\partial x_j} - \rho\overline{u_i' u_j'}\right) + S_j \quad \textbf{(1)}$$

where u_i and u_j denote the time-averaged values (i, j = 1, 2, 3) of the velocity component; p is the time-averaged value of the pressure; ρ is the fluid density; μ is the dynamic viscosity coefficient; $\rho\overline{u_i' u_j'}$ is the Reynolds stress term; and S_j is the source term.

TURBULENCE MODEL AND TREATMENT OF FREE SURFACE

The k-ω SST turbulence model proposed by Menter [12] was used to close the Reynolds stress term mentioned earlier. This turbulence model was chosen because it outperforms the standard k-w and standard k-epsilon models and offers desirable advantages when calculating the viscous flow field. This model is often used with the URANS method in marine applications, as it produces satisfactory results that are very close to reality [13-16]. The Volume of Fluid (VOF) method, proposed by Hirt and Nichols [17] and used in most commercial CFD codes, was chosen to capture the free surface. The VOF method entails analysing the boundaries between two or more incompatible media that do not mix. It is known for its capacity to monitor free liquid surfaces, requires minimal memory, and is simple to integrate [18]. Several instances of successful use of the VOF method in sea flows with free surfaces were demonstrated in published works [19-21], indicating that the method suits the problem in question.

VERIFICATION AND VALIDATION (V&V)

We conducted a V&V study using the methods proposed by Stern et al. [22-25], the International Towing Tank Conference, ITTC (2008) [26], and Xing and Stern (2010) [27]. Verification is the process in which the simulation of numerical uncertainty U_{SN} and the sign and magnitude δ^*_{SN} of the simulation numerical error are thoroughly assessed. $U^2_{SN} = U^2_I + U^2_T + U^2_G$, where U_I is the iterative uncertainty, U_T is the time-step uncertainty, and U_G is the grid uncertainty. U_T was not evaluated in this study due to a constant Courant–Friedrichs–Lewy number (CFL number) [28, 29]. In this study, the CFL number was set to 1. We analysed the iterative histories of tested parameters to determine iterative convergence. We estimated U_I as being half the range, between the maximum (S_U) and minimum (S_L) solution values for the oscillatory iterative convergence condition $U_I = \left|\frac{1}{2}(S_U - S_L)\right|$. Establishing the appropriate grid refinement ratio r_i of the i^{th} input parameter is necessary to conduct a grid convergence study. This ratio represents the relationship between the sizes of coarse and fine cells and is easy to calculate for a structured grid. However, in this study, only a structured grid was used, so we considered the grid refinement ratio to be $r_i = \frac{\Delta x_2}{\Delta x_3} = \frac{\Delta x_1}{\Delta x_2}$ [26], where the $\Delta x_{1,2,3}$ refer to the spacing of the fine, medium, and coarse grids. The Richard Extrapolation (ITTC, 2008) [26] was implemented to complete the grid-independent verification. The following equation was used to calculate the convergence ratio R_G, $R_G = \left|\frac{S_2 - S_1}{S_3 - S_2}\right|$, where S_1, S_2 and S_3 correspond to solutions with fine, medium, and coarse input parameters, respectively. The estimated error δ_G^* and order of accuracy P_G were calculated as:

$$\delta^*_{RE_G} = \frac{S_2 - S_1}{r_G^{P_G} - 1} \tag{2}$$

$$P_G = \frac{\ln\left((S_3 - S_2)/(S_2 - S_1)\right)}{\ln(r_G)} \tag{3}$$

where r_G is the refinement ratio (1.2 in the present work). Also, the ITTC (2008) demonstrated that using a multiplicative correction factor can be beneficial as a quantitative metric for several reasons: to determine the level of proximity of the solutions to the asymptotic range, establish the impact of higher-order terms, and estimate error and uncertainty margins. The error is defined as $\delta_G^* = C_G \times \delta^*_{RE_G}$, where C_G is the correction factor, which is defined as:

$$C_G = \frac{r_G^{P_G} - 1}{r_G^{P_{Gest}} - 1} \tag{4}$$

$P_{G_{est}}$ is the limiting order of accuracy of the first term as the spacing size approaches zero and $C_G \rightarrow 1$. The grid uncertainty was calculated using

$$U_G = \left(|C_G| + |1 - C_G|\right)\left|\delta^*_{RE_G}\right|, \quad C_G \geq 1$$
$$U_G = \left(2|1 - C_G| + 1\right)\left|\delta^*_{RE_G}\right|, \quad C\_G < 1 \tag{5}$$

If solutions are near the asymptotic range, C_G becomes close to 1 and δ_G^* is calculated as $\delta_G^* = C_G \times \delta^*_{RE_G}$, while U_{G_C} is estimated using $U_{G_C} = |1 - C_G|\left|\delta^*_{RE_G}\right|$, which has the correct form for both $C_G < 1$ and $C_G > 1$.

Validation is the process in which the simulation modelling uncertainty U_{SM} is assessed against benchmark experimental data D and, should the conditions allow, estimates the sign and magnitude of the modelling error δ_{SM} itself.

The difference between data D and the simulation result S is the comparison error E. If $|E| < U_V$, where U_V is the validation uncertainty ($U_V^2 = U_D^2 + U_{SN}^2$), where U_D is the experimental data uncertainty, then the validation is considered a success at the U_V level.

One of the key objectives of this study was to concentrate the wave energy within the proposed device, in order to operate a turbine that generates electricity; therefore, calculating the forces and moments affecting the turbine is very important. The MP687 propeller, which had experimental results for the open water test, was used as a turbine in the proposed device. The V&V procedure was conducted on the numerical results of the forces and moments affecting this propeller. The geometry of the MP687 propeller is illustrated in Fig. 1 and Table 1. The diameter of this propeller was 203 mm and the number of revolutions in the experiment was equal to 10.87 rps. The kinematic viscosity of water is 1.1213E-6 m^2/s, which corresponds to the Reynolds number 4.00E+05. The results of the open water test of the model propeller MP687 were published at the Tokyo Conference in 2015 [30].

High mesh quality is very important, to enable good results from CFD calculations [31, 32]. The mesh designed for this simulation consisted of rotating and static regions. Fig. 3 presents the grid in the stator and rotor domains. The stator mesh region was generated using the Ansys ICEM program; however, the rotor region was generated using both Ansys ICEM and the snappyHexMesh tool in OpenFOAM. The dynamic overset grid approach (implemented in the ANSYS-Fluent program) was used to model a discretised rotating propeller.

The V&V study of the propeller was carried out using three gradually refined grids (1.5, 2.6, and 4.48 million cells). A grid refinement was performed in the boundary layer near the propeller surface, see Fig. 3. The medium and fine grids were derived from the coarse grid as follows: the cell number in the computational domain was multiplied by a factor of 1.2 in the directions (x, y, z). The first computational node of all grids was located at $y^+ > 30$ from the wall.

Tab. 1. Propeller MP687 parameters [30]

Diameter	[m]	0.203
Pitch ratio, r/R = 0.7	[-]	0.75
Expanded area ratio	[-]	0.5
Angle of rake	[°]	5
Number of blades	[-]	5
Sense of rotation	[-]	Clockwise

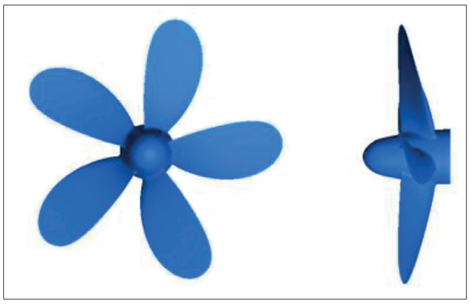

Fig. 1. The propeller MP687

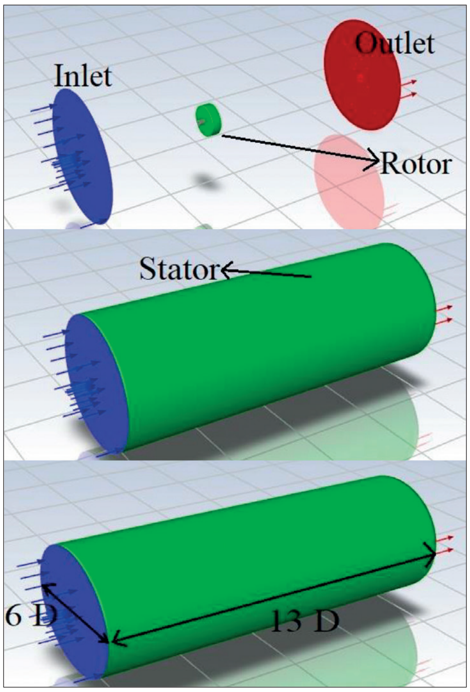

Fig. 2. The computational domain and boundary conditions of the open water test

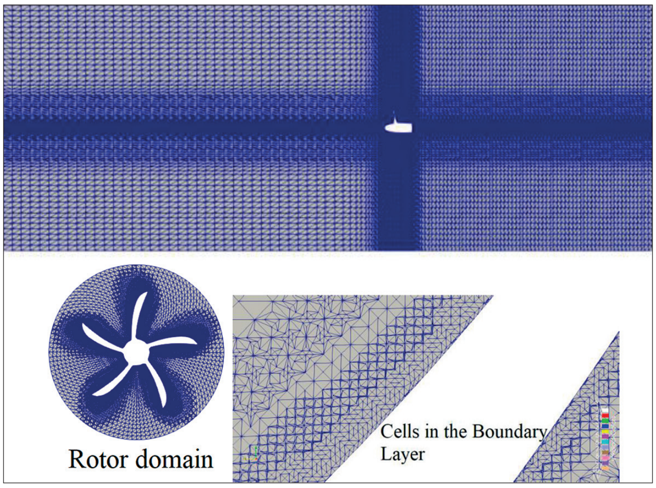

Fig. 3. The overall mesh domain of the open-water test

The coupled algorithm was used as the basis for the pressure-velocity coupling and solution procedure. Table 2 includes the settings that control the spatial discretisation of the convection terms in the solution equations.

Tab. 2. The numerical settings of the spatial discretisation of the convection terms

Gradient	Pressure	Momentum	Volume Fraction	Turbulent kinetic energy	Specific Dissipation Rate
Least Squares Cell-Based	PRESTO	Second Order Upwind	Compressive	Second Order Upwind	Second Order Upwind

The Verification and Validation procedure was applied to three parameters (thrust coefficient, K_T, torque coefficient, K_Q, and propeller efficiency, η_0) at the advance ratios of $J = 0.3$ (Table 3 and Table 4) and J=0.8 (Table 5 and Table 6). The value of the data uncertainty $U_D\%U$ was set to 1, in accordance with the recommendations of the Tokyo conference [33].

All results show monotonic convergence and the grid, simulation numerical, and validation uncertainty for K_T, K_Q, and η_0 is smaller than 5.5% S_1. Moreover, the error estimate δ^*_G is smaller than 3.5% S_1.

The experimental and numerical results exhibit similar trends of increasing and decreasing patterns based on the loading condition. Nonetheless, there is a slight difference in the force coefficient values between the experimental and CFD results. Hence, the chosen numerical approach is suiTable for examining the flow features beyond the rotating propeller and will be employed with the newly proposed device.

CONCEPT DEVELOPMENT

THE PROPOSED DEVICE

The proposed device was installed in the wave transition region, in which the water depth was $\frac{L}{2} > d > \frac{L}{20}$, see Fig. 7. The change from deep to shallow-water waves occurred when $d < \frac{L}{2}$. The trajectories of fluid particles are elliptical in shallow water. When the water depth was smaller than $\frac{L}{20}$, then there

Tab. 3. Hydrodynamic forces affecting the MP687 propeller at J = 0.3

Parameter	Exp	Coarse	Error%	Medium	Error%	Fine	Error%
K_T	0.2598	0.2400	7.621	0.2500	3.772	0.2520	3.000
$10K_Q$	0.3210	0.3000	6.542	0.3100	3.426	0.3120	2.800
η_0	0.3864	0.3819	1.164	0.3850	0.362	0.3856	0.204

Tab. 4. Verification and Validation of the hydrodynamic forces affecting the MP687 propeller at J = 0.3

Parameter	R_G	P_G	C_G	$U_G\%S_1$	$\delta^*_G\%S_1$	$U_{GC}\%S_1$	S_C	$U_D\%D$	$U_{SN}\%S_1$	$U_V\%S_1$
K_T	0.20	8.80	9.00	3.40	1.80	1.600	0.252	1	3.41	3.55
$10K_Q$	0.20	8.80	9.00	2.75	1.45	1.290	0.312	1	2.75	2.92
η_0	0.19	9.00	9.54	0.66	0.35	0.312	0.385	1	0.66	1.19

Tab. 5. Hydrodynamic forces affecting the MP687 propeller at J = 0.8

Parameter	Exp	Coarse	Error%	Medium	Error%	Fine	Error%
K_T	0.0353	0.0330	6.510	0.0340	3.680	0.0345	2.260
$10K_Q$	0.0921	0.0870	5.530	0.0890	3.360	0.0900	2.280
η_0	0.4879	0.4829	1.035	0.4864	0.320	0.4880	0.014

Tab. 6. Verification and Validation of the hydrodynamic forces affecting the MP687 propeller at J = 0.8

Parameter	R_G	P_G	C_G	$U_G\%S_1$	$\delta^*_G\%S_1$	$U_{GC}\%S_1$	S_C	$U_D\%D$	$U_{SN}\%S_1$	$U_V\%S_1$
K_T	0.50	3.80	2.27	5.13	3.29	1.844	0.035	1	5.13	5.23
$10K_Q$	0.50	3.80	2.27	3.93	2.52	1.410	0.091	1	3.93	4.06
η_0	0.48	3.98	2.43	1.23	0.77	0.450	0.489	1	1.23	1.58

were shallow water waves. A wave retains the bulk of its energy in the transitional region. In this device, the kinetic and potential energy of the flow is converted into electrical energy, as the turbine will be installed in the tunnel (see Fig. 4). More than one turbine can be installed in this device and a hemisphere can be added to the device to collect more wave energy, see Fig. 4. The device collects and focuses the wave energy by inserting a large amount of the wave at the device's inlet. The wave energy is harnessed by gradually decreasing the cross-sectional area of the passage through which the waves travel until they reach the tunnel outlet. In accordance with the principle of continuity, the wave celerity in the horizontal direction rises at the exit compared to its inlet, leading to a noTable enhancement in the turbine's efficiency and subsequent electric power generation.

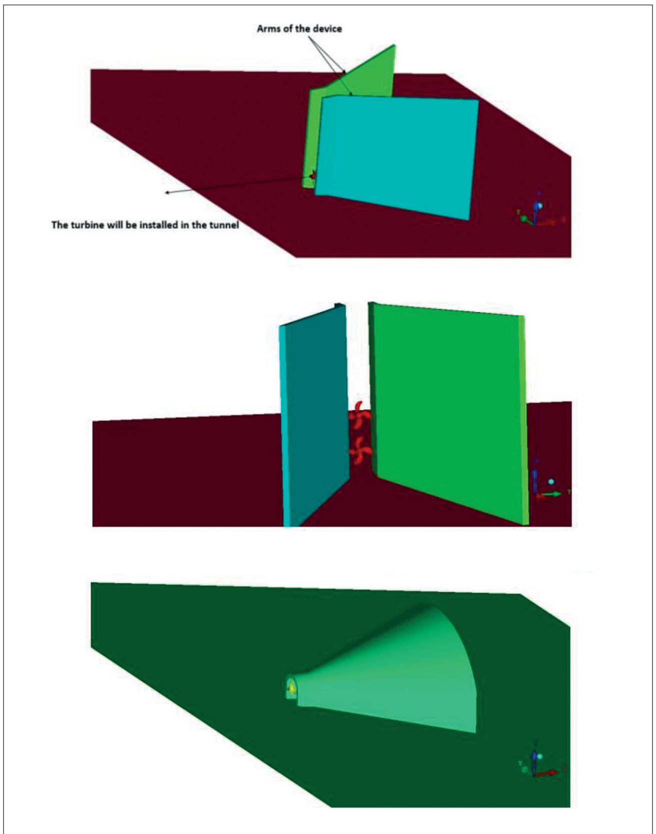

Fig. 4. The turbine will be installed in the tunnel

THE ADVANTAGES OF THE PROPOSED DEVICE COMPARED TO THE KNOWN WAVE DRAGON

The proposed device in this study is not similar to the Wave Dragon; it has the following differences:

- WD is moored (like a ship) in relatively deep water, i.e. more than 25 m [8], while the proposed device is fixed to the seabed in the transitional region, where the waves have 80% of their energy, see Fig. 7 [34]. Installing the device on the seabed makes it resistant to hurricanes.
- The air turbine can be fixed on the proposed device. The cost of foundations in wind turbines constitutes a large part of the total cost of the turbine; therefore, considering that the proposed device is made of environmentally friendly cement, it can be used as a foundation for the construction of wind turbines.
- The WD works on the potential energy of the water; the water collects in the reservoir and then passes through the turbine to the bottom, so that the potential energy contained in the water is converted into electricity, see Fig. 5. However, the proposed device works on turbulent kinetic energy, where the turbine located at the outlet of the device converts the turbulent kinetic energy of the wave into electrical energy. Also, in the proposed device, after taking advantage of the turbulent kinetic energy of the wave, water can be stored in a reservoir, and the potential energy of the water can be utilised, see Fig. 6.
  - In the proposed device, the arms are connected to the seabed and this will not allow the wave to leak from the bottom of the arms, as is the case with the WD.

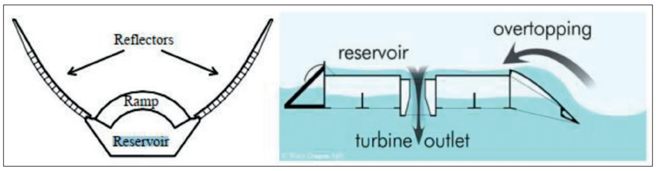

Fig. 5. Main components of the WD [8]

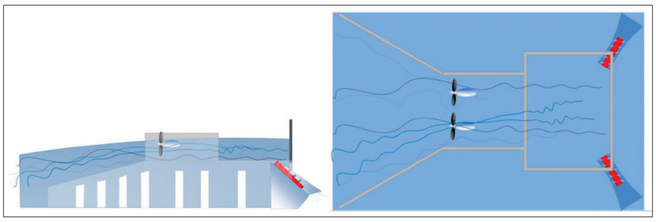

Fig. 6. Utilising the turbulent kinetic energy and potential energy of the wave in the proposed device

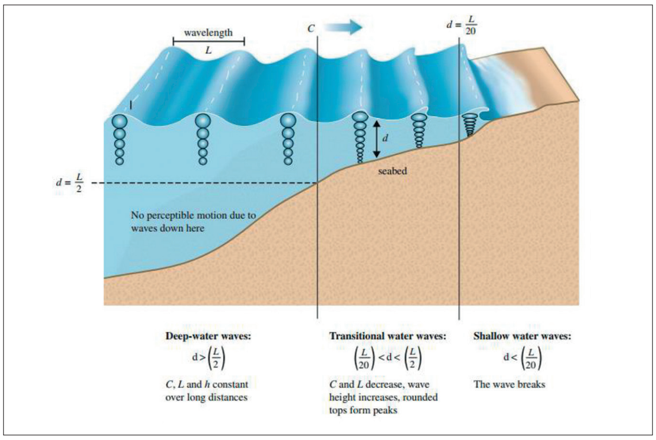

Fig. 7. Motion of water particles in deep and shallow water [34]

DEVICE GEOMETRY

Fig. 8 illustrates the geometry of the proposed device. Various scenarios have been computed, with variations in the arm angle, bottom angle, and the arm's length, see Table 7. In case 7, a hemisphere above the arms was added and the arm's height was reduced to the same level as the free surface. So, the proposed geometry is as shown in Fig. 9.

Tab. 7. Geometry of the proposed device

	Symbol	Case 1	Case 2	Case 3	Case 4	Case 5	Case 6	Case 7
Arm length	L [m]	15	15	15	8	8	8	8
Arm angle	β [°]	10.0	10.0	27.5	27.5	45.0	27.5	27.5
Beach angle	φ [°]	10	10	10	10	10	10	10
Tunnel width	a [m]	1	1	1	1	1	1	1
Tunnel length	b [m]	1	1	1	1	1	1	1

– Hemisphere height at the inlet = 2.8 m.
– Hemisphere height at the tunnel outlet = 0.5 m.

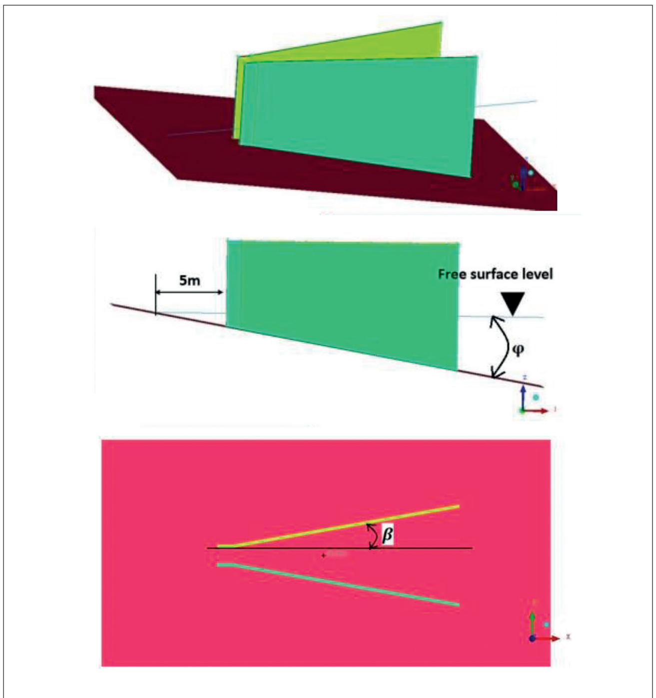

Fig. 8. Geometry of the proposed device

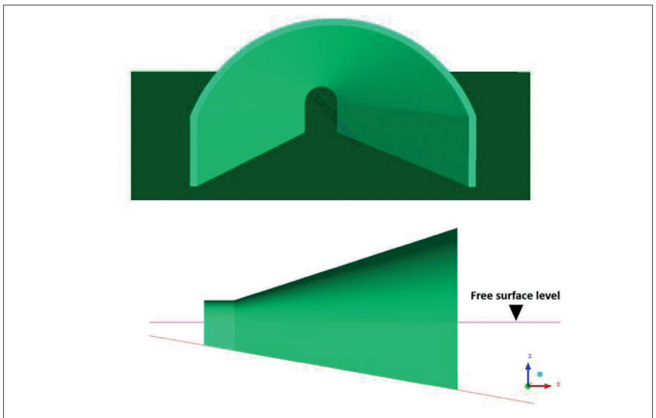

Fig. 9. Geometry of the proposed device, with hemisphere

NUMERICAL ENVIRONMENT AND BOUNDARY CONDITIONS

The new design considered the annual statistics of average wave height in Sweden. The information about waves in the western Sweden region was obtained from the official website of the Swedish Meteorological and Hydrological Institute (SMHI), which is concerned with climate matters. According to the SMHI, the annual average wave amplitude value is 1.1 m. The wavelength was calculated from this information using the Zimmerman equation [35], which can be written as:

$$H_f = 0.17 \times \lambda^{(3/4)} \quad (6)$$

where H_f is the wave height (m) and λ is the wavelength (m).

From SMHI data, the wave amplitude equals 1.1 m, so the wave height equals 2.2 m. Using Eq. (7), the wavelength will be equal to 30.38 m. These settings were used in case 1, see Table 8.

However, considering that the waves in the sea are non-sinusoidal, new waves were generated in cases 2-7, which is a sum of three different sinus waves with the following setting (see Table 8).

Tab. 8: Wave setting in the proposed design

Case number	Wavenumber	Wavelength [m]	Wave height [m]	Phase difference [°]
1	1	30.38	2.2	0
2,3,4,5,6,7	1	30.38	2.2	0
	2	23.25	1.8	30
	3	15.66	1.3	60

A fine-structured grid with 6 million cells was used to achieve the CFD calculation, see Fig. 10. $y^+ > 30$ and the same numerical settings in Table 2 were used to achieve the spatial discretisation of the convection terms. The complete numerical simulation boundary conditions, settings, solver controls, convergence targets, residuals, and time step settings are provided in Table 9 and Table 10.

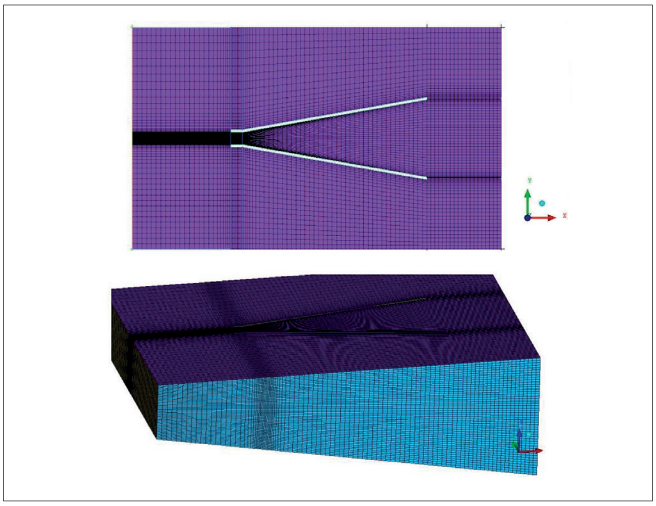

Fig. 10. Structured grid for the solution domain

Tab. 9. Detailed numerical simulation parameters

(a) Solver		(b) VOF Model		(c) Boundary Conditions	
Type	Pressure based	VOF-Water	0.5	Bottom and Arms	No-slip wall
Velocity formulation	Absolute	VOF-Air	0.5	Inlet	Velocity-inlet Open Channel Wave BC Additional settings in Table 10
Time	Transient	Homogeneous Models	Volume Of Fluid	Outlet	Pressure Outlet Multiphase: Open Channel Pressure Specification Method-Free Surface Level Free Surface Level [m] 0 Bottom Level [m]/-100 Density Interpolation Method-From Free Surface Level
Simulation time	20 [s]	Volume Fraction Parameters	Formulation-Implicit	Turbine	Wall-Moving Wall Motion: Relative to the Adjacent Cell Zone Components-Velocity Components X-Velocity [m/s] 0 Y-Velocity [m/s] 0 Z-Velocity [m/s] 0
Time step size	0.0005 [s]	VOF sub-Models	Open Channel Flow Open Channel WB	Top	Opening
Number of time step	40000	Interface modelling-type	Sharp	Overset interface between rotor and stator	Overset
Maximum iterations	10	Body force formulation	Implicit Body Force	(d) Overset Interfaces	
Convergence Target Residual	0.00001	Air-primary phase	Phase material – air	Background Zones	Stator
Gravity	ON	Water – secondary phase	Phase material – water-liquid	Component Zones	Rotor
Multiphase	Mixture model VOF	Phase Interaction	Air Water	(e) Dynamic Mesh	
Fluids	Air and Water	Surface Tension Coefficient (N/m)	Constant-0.073	Options	Six DOF
		Global Options	Surface tension force modelling	Six DOF Properties	Name: rotation-function One DOF Rotation Mass [kg] 15.677 Centre of Rotation and Moment of Inertia [kg/m^2] must be given
	Turbulence Model	Shear Stress Transport (SST)			

(g) Dynamic Mesh Zones	
Stator cell zone	Stationary
Rotor cell zone	Rigid Body Six DOF UDF/Properties-rotation-function Six DOF: On and Passive Centre of Gravity Location must be given
Overset interface	Rigid Body Six DOF UDF/Properties-rotation-function Six DOF: On and Passive Centre of Gravity Location must be given
Turbine	Rigid Body Six DOF UDF/Properties-rotation-function Six DOF: On Centre of Gravity Location must be given

Fig. 11 illustrates the boundary faces of the solution domain. The wave is entered from the inlet.

RESULTS AND DISCUSSION

With the new design, we focused on the mass flow rate of incoming water to the assembler inlet and the mass flow rate of outgoing water. Furthermore, we focused on each wave's energy rate per metre in the Y-direction upon entry and exit (the Y-direction is in the horizontal plane perpendicular to the

Tab. 10. Additional settings for inlet boundary condition

Inlet	Velocity-inlet Open Channel Wave BC
Multiphase	Secondary Phase for Inlet-Water Wave BC Options-Shallow/Intermediate Waves Free Surface Level [m]-0 Bottom Level [m]/-100 Reference Wave Direction-Averaged Flow Direction Wave Modelling Options-Wave Theories
Wave Group Inputs	Number of Waves=1 for case 1 and =3 for cases 2-7
Case 1	
Wave-1	Wave Theory-Third Order Stokes Wave Height [m] 2.2 Wave Length [m] 30.38 Phase Difference [deg] 0 Wave Heading Angle [deg] 0
Cases 2-7	
Wave-1	Wave Theory-Third Order Stokes Wave Height [m] 2.2 Wave Length [m] 30.38 Phase Difference [deg] 0 Wave Heading Angle [deg] 0
Wave-2	Wave Theory-Third Order Stokes Wave Height [m] 1.8 Wave Length [m] 23.25 Phase Difference [deg] 30 Wave Heading Angle [deg] 0
Wave-3	Wave Theory-Third Order Stokes Wave Height [m] 1.3 Wave Length [m] 15.066 Phase Difference [deg] 60 Wave Heading Angle [deg] 0

line of wave propagation; see Fig. 10). The energy rate per metre in the Y-direction was the designated criteria for evaluating the design quality. As mentioned earlier, the mass flow was calculated on the inlet, outlet, and the middle plane (located 5 m after the inlet). The three planes are shown in Fig. 12.

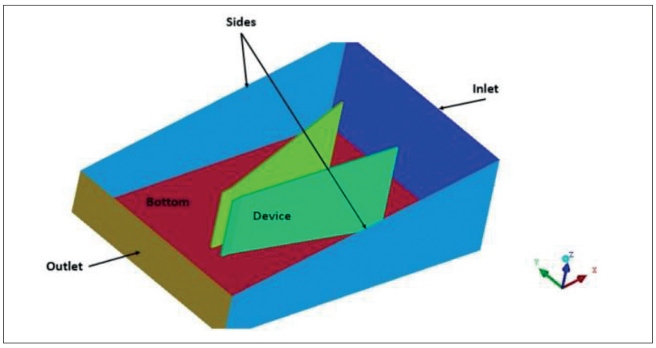

Fig. 11. Boundary faces of the solution domain

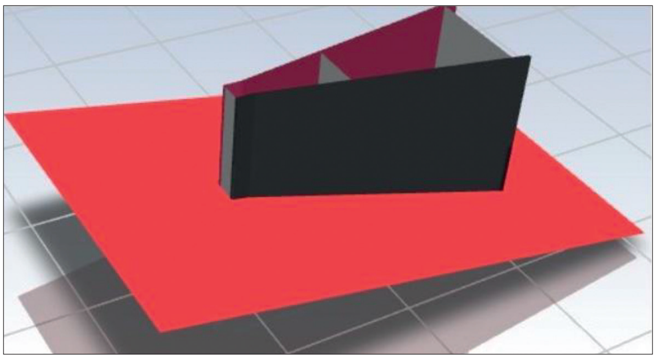

Fig. 12. Three transversal planes at which the mass flow rate was calculated

MASS FLOW RATE

Fig. 13 demonstrates the water mass flow rate in each of the three planes in Case 1. The figure shows that the regressing flow significantly decreases at the outlet compared to its value at the inlet. It should also be noted that 25% of the incoming wave (along the entire inlet width) arrives and exits the 1-metre-wide outlet. Fig. 14 demonstrates the water mass flow rate in each of the three planes in Cases 2-7. It shows that the largest mass flow rate at the inlet occurs in cases 3 and 6. In case 6, the bottom angle equals 20 degrees. Fig. 14 shows that this bottom angle causes a large amount of regressing flow at the outlet, which is undesirable. In Case 3, the arm's length is 15 m, which leads to significant forces affecting the arms. The same situation occurs in Cases 2 and 5. The arm's angle in Case 5 is 45o, leading to significant transversal and axial forces affecting the device.

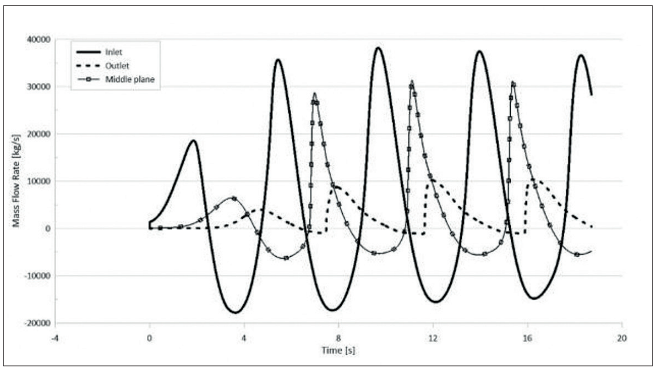

Fig. 13. Water mass flow rate in each of the three planes: inlet, outlet, and middle plane in Case 1

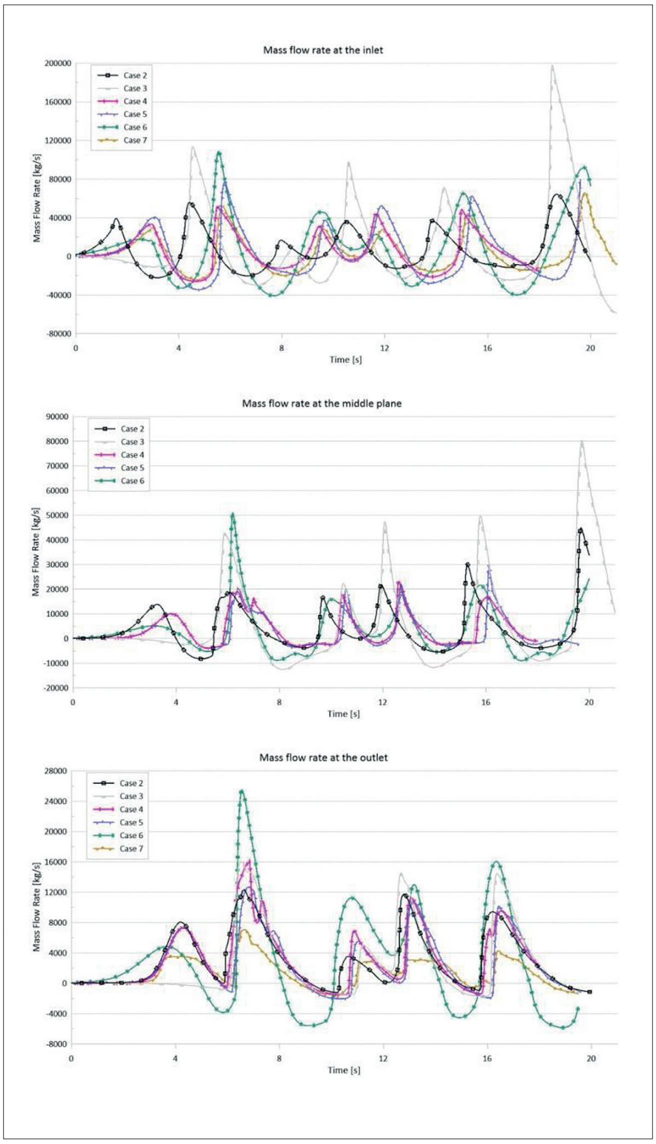

Fig. 14. Mass flow rate for all cases

Fig. 15 shows the exit of the third wave from the tunnel (in Case 7). As shown in this figure, the velocity of the water is equal to 9-10 m/s. Analysing these results shows that 9-18% of the inlet mass flow arrives at the outlet; the average value of the mass flow at the outlet is 12.4% of the inlet mass flow.

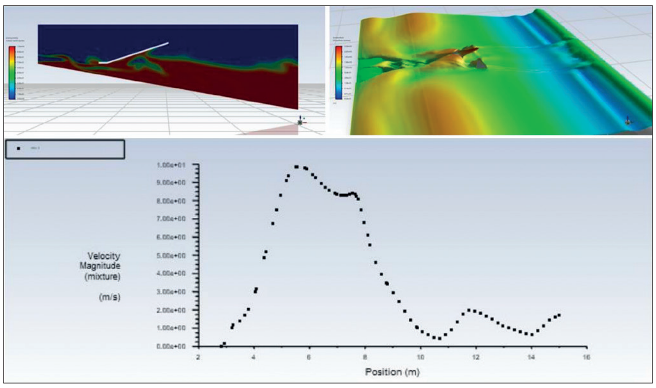

Fig. 15. The exit of the third wave from the device

TURBULENT KINETIC ENERGY

The wave speed at the outlet is larger than at the inlet; thus, the turbulent kinetic energy rate was calculated using the following equation:

$$TKE = \frac{1}{2}\dot{m}V^2 \tag{7}$$

where $\dot{m}$ is the mass flow rate $[\frac{Kg}{s}]$ and V is the averaged value of the wave velocity in each considered plane $[\frac{m}{s}]$.

Fig. 16 illustrates the energy rate of the waves at the three planes in Case 1. Fig. 17 shows the TKE of the waves for the three planes in the other cases. The energy rate per metre in the transversal direction (Y-direction) was determined by calculating the area under the curve above the X-axis, which represents the total TKE of the wave mass, and then dividing it by the plane's width in the Y-direction. Accordingly, the results are shown in Table 11, which indicates that the energy rate of the output wave per cross meter, perpendicular to the wave propagation, is between 200-1200% of the energy rate of the input wave per cross meter. The wavenumber in this Table refers to the number of waves transmitted through the device. By taking the mean value of the percentage energy concentration at the outlet, we can see that the best results were obtained in Case 3, where the mean value of the energy concentration per cross meter at the outlet is 725% of the cross meter at the inlet. In the first case, the value was 236%. In Cases 2, 4, and 5, the energy concentration is approximately 400%. In Case 6, the energy concentration reaches 525%. In Case 7, we note that there is no improvement in the energy concentration compared to the other cases, as the energy concentration value does not exceed 290%. In Case 6, there is a large amount of flow regression on the outlet; the arms are relatively long in Case 3, so Case 4 was chosen in order to add the propeller within the three planes and make sure of the possible benefit of concentrating the wave energy within the proposed device.

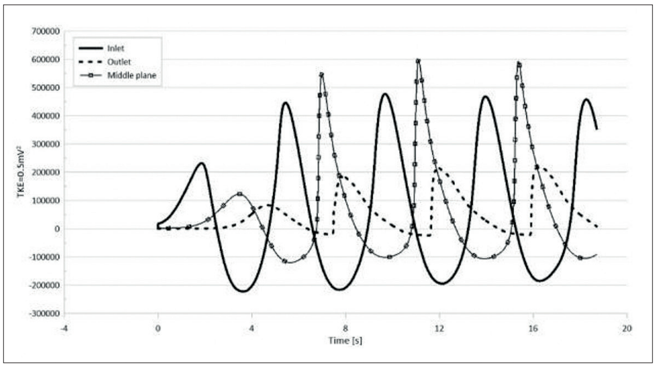

Fig. 16. Energy rate in each of the three planes

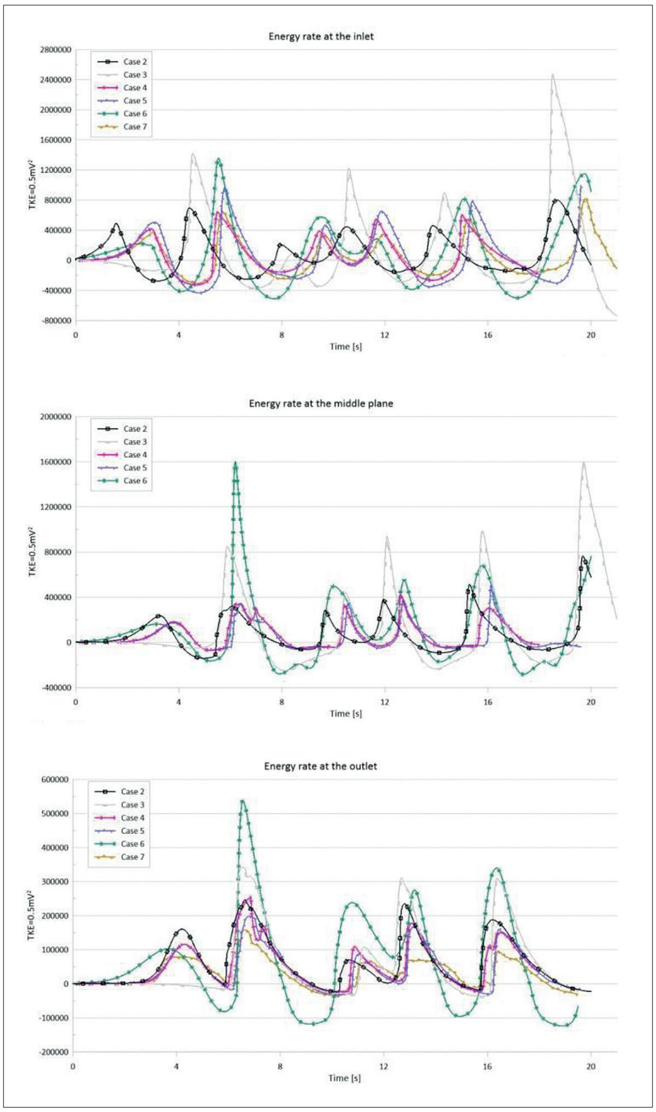

Fig. 17. Energy rate for all cases

ADDING THE MP687 PROPELLER TO CASE 4

The propeller was added to the proposed device in Case 4 in three different forms:
– the propeller was placed in the open sea without the device,
– the propeller was placed in the middle level of the device,
– the propeller was placed at the device's outlet.

By performing the calculations, it is possible to predict the approximate value of the energy concentration using the proposed device. The MP687 propeller was used as a turbine. In all previous cases, structured grids were used and it was assumed that, initially, the propeller was totally submerged in water. An aluminium propeller with a diameter of 70 cm was used, with a mass 15.677 kg. The inertia moments of the propeller were calculated using the static structure program in the Ansys program. Also, as in the open water test, the dynamic overset grid approach was used to model a discretised rotating propeller. The User Defined Function (UDF) technique (available in the Fluent program) was used to set the propeller to a single degree of freedom, so that it could rotate due to the forces acting on it from the waves.

The same waves were used as in the previous cases, see Table 8 and the torque acting on the propeller and angular velocity were calculated. Thus, the expected power was calculated using this propeller with the proposed device in Case 4. The angular velocity [rad/s] was multiplied by the moment exerted on the propeller [N.m] to determine the amount of electrical power it generates. Fig. 18 shows the moment acting on the propeller in the three positions. This figure clearly shows that the moment affecting the propeller inside the device is better than in the case of the open sea, and this confirms that the device plays a positive role in enhancing the wave energy. Moreover, considering that a large moment will lead to a large angular velocity, we can see an improvement in the electric power at the outlet compared to the middle plane, see Fig. 18.

The results presented in Fig. 18 confirm that the proposed device concentrates the energy of the waves compared to the case of the open sea (without the device's presence). These results also confirm that the turbine's best productivity is when it is located at the device outlet.

Through the above, it can be said that the advantages of the proposed device are as follows:
– The proposed device is installed in the transition region, where the wave retains more than 80% of its energy.
– The kinetic energy of the wave is utilised.
– Wave energy can be harvested regardless of wave height.
– Arm height can be adjusted above the free surface, in proportion to the annual mean height of the waves in the area in which the device is installed, and the aim is to take advantage of the largest part of the wave energy.

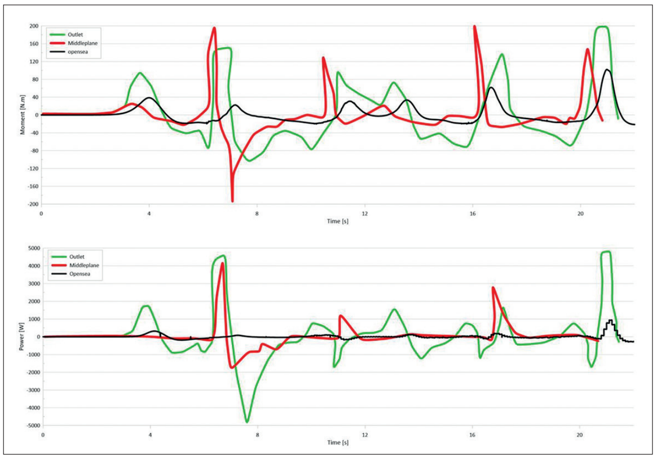

Fig. 18. The moment acting on the propeller in the three positions and the energy produced by the propeller due to the effect of this moment

As the device will be installed in the ocean, it is reasonable to expect that it will impact marine activities and the ocean environment. Potential concerns include the disruption of marine ecosystems, the environmental impact, and endangering marine traffic. It is also advised that such devices are installed in places dedicated to harvesting wave energy and, therefore, have minimal ship and/or boat traffic. As a result, the electrical connection is more straightforward and cheaper, the design is not complex, and the cost of construction and operation is lower.

Tab. 11. Energy rate in the three planes for all cases

Wavenumber	inlet TKE	TKE/m	5m TKE	TKE/m	outlet TKE	TKE/m	outlet/inlet%
Case 1							
2	33163.800	5273.303	24254.000	8778.140	12004.000	12004.000	228
3	38881.200	6182.414	29353.000	10623.600	14746.000	14746.000	238
4	37880.600	6023.311	30137.000	10907.350	14580.000	14580.000	242
Case 2							
1	537326.710	85439.130	292937.800	106021.600	226737.000	226737.000	265
2	527605.380	83893.370	372551.000	134835.700	408345.000	408345.000	487
3	119600.123	19017.350	212424.000	76881.650	64970.000	64970.000	342
4	446806.920	71045.780	349256.000	126404.600	321031.000	321031.000	452
5	406777.900	64680.860	507835.000	183798.400	282967.000	282967.000	437
Case 3							
1	1306407.110	93314.790	776088.600	154722.600	488782.359	488782.400	524
2	956573.270	68326.660	715955.400	142734.300	349975.759	349975.800	512
3	818060.068	58432.860	784913.900	156482.000	422683.361	422683.400	723
4	2390609.908	170757.900	1551287.000	309267.700	1130026.368	1130026.000	661
5	1810995.429	129356.800	1422182.000	283529.100	1556687.054	1556687.000	1203
Case 4							
1	622084.187	74411.980	239781.600	86563.760	187447.449	187447.400	252
2	503567.785	60235.380	394023.300	142246.700	394297.568	394297.600	655
3	269660.140	32256.000	184085.700	66456.930	102409.190	102409.200	317
4	433402.621	51842.420	323071.200	116632.200	201351.138	201351.100	388
5	602452.752	72063.730	293929.100	106111.600	200709.325	200709.300	278
Case 5							
1	801890.741	65194.370	229017.000	65809.490	185717.778	185717.800	285
2	685881.151	55762.700	333177.200	95740.570	271899.785	271899.800	487
3	236966.796	19265.590	157713.800	45320.070	79835.127	79835.130	414
4	566630.608	46067.530	306429.100	88054.350	193590.976	193591.000	420
5	716727.485	58270.530	359228.500	103226.600	197422.535	197422.500	338
Case 6							
1	357380.290	42748.840	313307.100	113107.300	178471.461	178471.500	417
2	1012603.106	121124.800	1100463.000	397279.100	478620.722	478620.700	395
3	605805.160	72464.730	531462.600	191863.800	266529.367	266529.400	367
4	195319.821	23363.620	518494.400	187182.100	252936.298	252936.300	1082
5	758951.004	90783.610	572694.300	206748.800	326279.359	326279.400	360
Case 7							
1	476165.308	55626.790	-	-	117651.000	117651.000	211
2	475061.048	55497.790	-	-	199975.783	199975.800	360
3	273342.531	31932.540	-	-	49656.054	49656.050	155
4	289982.074	33876.410	-	-	90636.089	90636.090	267
5	411534.710	48076.480	-	-	99228.402	99228.400	206
6	675213.067	78880.030	-	-	195211.806	195211.800	247
7	464430.442	54255.890	-	-	242823.547	242823.500	447
8	448041.927	52341.350	-	-	249139.416	249139.400	476

CONCLUSION

In this paper, a new device for harvesting wave energy is proposed. The Computational Fluid Dynamics (CFD) method was used to achieve the purpose of this work. The accuracy of the CFD results is confirmed by comparing them with experimental data. The study examines different design parameters of the proposed WEC, highlighting the significant impact of the device's arms and bottom angle on its performance. In contrast to the floating Wave Dragon system situated in deep waters to utilise potential energy, the new fixed-seabed device is positioned in the nearshore transitional wave zone, where waves retain a substantial amount of their energy. The MP687 turbine was utilised to collect the wave energy in three locations: in the open sea, at the centre of the device, and at the device's outlet. Results demonstrate that the device effectively concentrates wave energy, particularly when the turbine is placed at the outlet. The proposed WEC offers several benefits, such as its fixed location in a high-energy wave area, effective utilisation of turbulent kinetic energy, and durable construction capable of withstanding severe weather conditions.

Future research should explore new turbine designs and configurations, to utilise wave energy fully. It is also essential to use more than one turbine in one device, where it is possible to place two turbines at the outlet, one under the free surface and the other above it. This means that it is possible to benefit more from the energy of one wave since, in this study, only the energy of the wave was used in the lower part, where the turbine is located. In contrast, the upper part of the wave came out of the device without using its power.

The study concludes that the device's environmental benefits, cost-effectiveness, and improved energy capture make it a promising solution for renewable energy generation.

REFERENCES

1. [Ellabban O, Abu-Rub H, Blaabjerg F. Renewable energy resources: Current status, future prospects and their enabling technology. Renewable and Sustainable Energy Reviews, vol. 39. 2014, doi: 10.1016/j.rser.2014.07.113.
2. Roy NK, Das A. Prospects of Renewable Energy Sources. pp. 1–39, 2018, doi: 10.1007/978-981-10-7287-1_1.
3. Clément A, McCullen P, Falcão A, Fiorentino A, Gardner F, Hammarlund K, Lemonis G, Lewis T, Nielsen K, Petroncini S, Pontes MT, Schild P, Sjöström BO, Sørensen HC, Thorpe T. Wave energy in Europe: current status and perspectives. Renew. Sustain. Energy Rev. vol. 6, no. 5, pp. 405–431, Oct. 2002, doi: 10.1016/S1364-0321(02)00009-6.
4. Guo B, Ringwood JV. Geometric optimisation of wave energy conversion devices: A survey. Appl. Energy, vol. 297, p. 117100, Sep. 2021, doi: 10.1016/J.APENERGY.2021.117100.
5. Kofoed JP. Optimisation of Overtopping Ramps for Utilisation of Wave Energy. Hydraulics & Coastal Engineering Laboratory, Department of Civil Engineering, Aalborg University, p. 94, 2000, [Online]. Available at: https://vbn.aau.dk/files/54592444/Optimisation_of_Overtopping_Ramps_for_Utilisation_of_Wave_Energy.pdf.
6. Kofoed JP. Wave Overtopping of Marine Structures: utilisation of wave energy. Hydraulics & Coastal Engineering Laboratory, Department of Civil Engineering, Aalborg University, p.191, 2002. [Online]. Available at: https://vbn.aau.dk/ws/files/316397223/Wave_Overtopping_of_Marine_Structures_utilisation_of_wave_energy.pdf.
7. Victor L, Troch P, Kofoed JP. On the Effects of Geometry Control on the Performance of Overtopping Wave Energy Converters. Energies 2011, Vol. 4, Pages 1574-1600, vol. 4, no. 10, pp. 1574–1600, Oct. 2011, doi: 10.3390/EN4101574.
8. Kofoed JP, Frigaard P, Friis-Madsen E, Sørensen HC. Prototype testing of the wave energy converter wave dragon. Renewable Energy, vol. 31, no. 2, 2006. doi: 10.1016/j.renene.2005.09.005.
9. Falcão AFdO. Wave energy utilisation: A review of the technologies. Renew. Sustain. Energy Rev., vol. 14, no. 3, pp. 899–918, Apr. 2010, doi: 10.1016/J.RSER.2009.11.003.
10. Parmeggiani S, Kofoed JP, Friis-Madsen E. Experimental Update of the Overtopping Model Used for the Wave Dragon Wave Energy Converter. Energies 2013, Vol. 6, Pages 1961-1992, vol. 6, no. 4, pp. 1961–1992, Apr. 2013, doi: 10.3390/EN6041961.
11. Martins JC, Goulart MM, Gomes MN, Souza JA, Rocha LAO, Isoldi LA, Santos ED. Geometric evaluation of the main operational principle of an overtopping wave energy converter by means of Constructal Design. Renew. Energy, vol. 118, pp. 727–741, Apr. 2018, doi: 10.1016/J.RENENE.2017.11.061.
12. Menter FR. Two-equation eddy-viscosity turbulence models for engineering applications. AIAA J., vol. 32, no. 8, pp. 1598–1605, Aug. 1994, doi: 10.2514/3.12149.
13. Abbas N, Kornev N, Shevchuk I, Anschau P. CFD prediction of unsteady forces on marine propellers caused by the wake nonuniformity and nonstationarity. Ocean Eng. 2015, doi: 10.1016/j.oceaneng.2015.06.007.
14. Abbas N, Kornev N. Study of unsteady loadings on the propeller under steady drift and yaw motion using URANS, hybrid (URANS-LES) and LES methods. Sh. Technol. Res., vol. 63, no. 2, pp. 121–131, May 2016, doi: 10.1080/09377255.2016.1211582.
15. Kornev N, Abbas N. Numerical Simulation of the tip vortex behind a wing oscillated with a small amplitude. J. Aircr., vol. 54, no. 2, 2017, doi: 10.2514/1.C033945.
16. Abbas N, Kornev N. Validation of hybrid URANS/LES methods for determination of forces and wake parameters

of KVLCC2 tanker at manoeuvring conditions. Sh. Technol. Res., vol. 63, no. 2, pp. 96–109, May 2016, doi: 10.1080/09377255.2016.1157275.

17. Hirt CW, Nichols BD. Volume of fluid (VOF) method for the dynamics of free boundaries. J. Comput. Phys., vol. 39, no. 1, pp. 201–225, Jan. 1981, doi: 10.1016/0021-9991(81)90145-5.

18. Wei Song K, yu Guo C, Wang C, Sun C, Li P, fan Zhong R. Experimental and numerical study on the scale effect of stern flap on ship resistance and flow field. Ships Offshore Struct., vol. 15, no. 9, 2019, doi: 10.1080/17445302.2019.1697091.

19. Lee H, Rhee SH. A dynamic interface compression method for VOF simulations of high-speed planing watercraft. J. Mech. Sci. Technol., vol. 29, no. 5, pp. 1849–1857, May 2015, doi: 10.1007/S12206-015-0405-6/METRICS.

20. Queutey P, Visonneau M. An interface capturing method for free-surface hydrodynamic flows. Comput. Fluids, vol. 36, no. 9, pp. 1481–1510, Nov. 2007, doi: 10.1016/J.COMPFLUID.2006.11.007.

21. Rhee SH, Makarov BP, Krishinan H, Ivanov V. Assessment of the volume of fluid method for free-surface wave flow. J. Mar. Sci. Technol., vol. 10, no. 4, pp. 173–180, Dec. 2005, doi: 10.1007/S00773-005-0205-2/METRICS.

22. Stern F, Wilson RV, Coleman HW, Paterson EG. Verification and validation of CFD simulations. Proc. 1999 3rd ASME/JSME Jt. Fluids Eng. Conf. FEDSM'99, San Fr. California, USA, 18-23 July 1999, 1999.

23. Stern F, Wilson RV, Coleman HW, Paterson EG. Comprehensive approach to verification and validation of CFD simulations—Part 1: Methodology and procedures. J. Fluids Eng. Trans. ASME, vol. 123, no. 4, 2001, doi: 10.1115/1.1412235.

24. Wilson RV, Stern F, Coleman HW, Paterson EG. Comprehensive approach to verification and validation of CFD simulations—Part 2: Application for rans simulation of a cargo/container ship. J. Fluids Eng. Trans. ASME, vol. 123, no. 4, 2001, doi: 10.1115/1.1412236.

25. Stern F, Wilson R, Shao J. Quantitative V&V of CFD simulations and certification of CFD codes. Int. J. Numer. Methods Fluids, vol. 50, no. 11, pp. 1335–1355, Apr. 2006, doi: 10.1002/FLD.1090.

26. ITTC. Uncertainty Analysis in CFD Verification and Validation Methodology and Procedures. 25th International Towing Tank Conference. pp. 1–12, 2008, [Online]. Available: https://www.ittc.info/media/8153/75-03-01-01.pdf.

27. Xing T, Stern F. Factors of safety for Richardson extrapolation. J. Fluids Eng. Trans. ASME, vol. 132, no. 6, pp. 614031–640313, Jun. 2010, doi: 10.1115/1.4001771/456309.

28. Ali MSM, Doolan CJ, Wheatley V. Grid convergence study for a two-dimensional simulation of flow around a square cylinder at a low Reynolds number. In: Seventh International Conference on CFD in the Minerals and Process Industries, CSIRO, Melbourne, Australia, [Online]. Available: https://flair.monash.edu/intranet/proceedings/cfd2009/PDFs/136ALI.pdf.

29. Koo B, Yang J, Yeon SM, Stern F. Reynolds and froude number effect on the flow past an interface-piercing circular cylinder. Int. J. Nav. Archit. Ocean Eng., vol. 6, no. 3, pp. 529–561, Sep. 2014, doi: 10.2478/IJNAOE-2013-0197.

30. Tokyo-2015. Open Water Tests for JBC (NMRI) MODEL PROPELLER NO.687. 2015, Accessed: 28-Jun-2023. [Online]. Available: https://www.t2015.nmri.go.jp/Instructions_JBC/instruction_JBC_files/Open_Water_Tests_for_JBC_NMRI.txt

31. Weerakoon AHS, Thilan W, De Silva HA, Assadi M. Fixed type-oscillating water column front wall angle variation and impact on chamber performance: CFD numerical wave tank assessment. IOP Conf. Ser. Mater. Sci. Eng., vol. 1294, no. 1, p. 012015, Dec. 2023, doi: 10.1088/1757-899X/1294/1/012015.

32. Alkhabbaz A, Yang HS, Weerakoon AHS, Lee YH. A novel linearization approach of chord and twist angle distribution for 10 kW horizontal axis wind turbine. Renew. Energy, vol. 178, pp. 1398–1420, Nov. 2021, doi: 10.1016/J.RENENE.2021.06.077.

33. Tokyo-2015. A Workshop on CFD in Ship Hydrodynamics. Accessed: 28-Jun-2023. [Online]. Available: https://t2015.nmri.go.jp/jbc.html.

34. Folley M. The Wave Energy Resource. Springer, Cham, pp. 43–79, 2017, doi: 10.1007/978-3-319-39889-1_3.

35. Sichkarev VI, Palagushkin BV. Conversion of the wavelength distribution to the energy spectrum of the wave. J. Phys. Conf. Ser., vol. 2131, no. 5, p. 052055, Dec. 2021, doi: 10.1088/1742-6596/2131/5/052055.